ORIGINAL ARTICLE

Nitrogen and phosphorous co-doped carbon nanotubes for high-performance supercapacitors

Johnsirani Devarajan[1] · Pandurangan Arumugam[1]

Abstract

Nitrogen and phosphorous dual-doped carbon nanotubes (N,P/CNT) have been grown in a single-step direct synthesis process by CVD method using iron-loaded mesoporous SBA-15 support, as an electrode material for the energy storage device. For comparison, pristine nanotubes, nitrogen and phosphorous individually doped nanotubes were also prepared. The basic characterization studies clarify the formation of nanotubes and the elemental mapping tells about the presence of the dopant. Under three-electrode investigations, N,P/CNT produced a maximum specific capacitance of about 358.2 F/g at 0.5 A/g current density. The electrochemical performance of N,P/CNT was further extended by fabricating as a symmetric supercapacitor device, which delivers 108.6 F/g of specific capacitance for 0.5 A/g with 15 Wh/kg energy density and 250 W/kg power density. The observed energy efficiency of the device was 92.3%. The capacitance retention and coulombic efficiency were 96.2% and 90.6%, respectively, calculated over 5000 charge–discharge cycles.

Graphical abstract
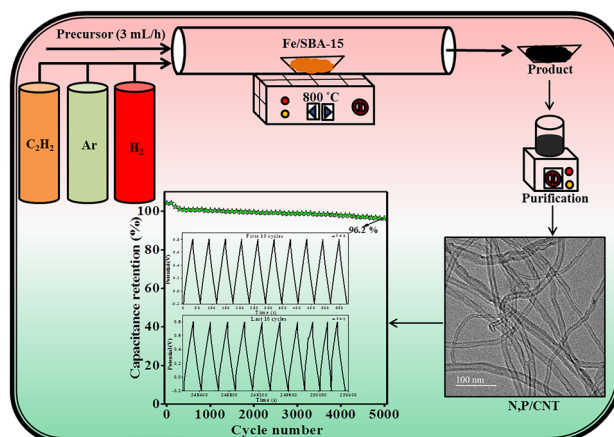
✉ Pandurangan Arumugam
pandurangan_a@yahoo.com

1   Department of Chemistry, College of Engineering Guindy,
    Anna University, Chennai, Tamilnadu 600025, India

1 Introduction

In recent days, nanostructured materials having dimensions less than 100 nm are of great interest, worldwide, owing to their improved properties with that of bulk materials. Carbon is one of the most abundant elements present on the earth crust and has been a source of energy to human society for thousands of year. Carbon-based nanostructured

materials are extensively used in many areas of applications such as sensors, catalysis, drug delivery and energy storage due to their intrinsic structure, electrical property, mechanical property and compatibility with biological systems. The various structural arrays of carbon-based nanomaterials are fullerene, graphene, carbon nanotubes, diamond and amorphous carbon [1–3].

Carbon nanotubes (CNTs) were discovered in 1991, from that onwards a huge area of research has been going-on because of their unique properties [4]. Also, recent research reports that CNTs were present in the black coatings of the inner walls of pottery shards, dates back sixteenth to eighteenth century, excavated from Keeladi, Tamilnadu [5]. The extraordinary thermal and chemical stability of CNTs favors them in the field of energy storage. Many literatures have been published using CNT-based electrode materials for supercapacitors [6]. The supercapacitor performance of the nanotubes can be modified by creating defects or adding foreign atoms to their crystalline structure [7]. Further doping the carbon materials with heteroatoms like B, N, P and S are found to be useful in modifying the electrochemical performance. These non-carbon atoms with different electronic size and electronegativity are significantly altering the electronic properties of the nanotubes when included in their hexagonal network [8, 9]. Nitrogen doping enables the electron transfer in the carbon material by causing a shift in the Fermi level and increase the capacitance by improving the wettability of the carbon surface in the electrolyte [10]. Phosphorous doping is also found to be effective in nanotubes either as a single dopant or as a co-dopant with nitrogen [11]. In addition, co-doping non-carbon atoms can be found to be impactful in improving the capacitance of the carbon material due to the synergetic effect [12].

The methods used for the production of carbon nanotubes for supercapacitors mainly include chemical vapour deposition (CVD), laser abalation and arc discharge. Among these methods, CVD is considered to be a promising and excellent technique for the synthesis of mass production of high-purity CNTs at low cost with easy scalability, in which temperature, catalyst and support play an important role. The catalyst aids as a seed for the growth of CNTs and transition metals like Fe, Ni, Co, Cr, V, Mo and Pd are generally preferred. It was reported that the iron catalyst produce best quality CNTs with high density and small diameter [13–16]. Along with the catalyst, the support also plays a role in the growth mechanism. Silica, mesoporous molecular sieves, zeolites calcium carbonate or magnesium oxide are usually favored as the catalyst support [17]. The unique properties of mesoporous molecular sieves such as lightweight, specific surface area, pore size, thermal stability and extending framework structure, make them selective for the growth of CNTs. Santa Barbara Amorphous-15 (SBA-15) is one of the mesoporous molecular sieve with hexagonally ordered

mesopores, thicker pore walls and higher hydrothermal stability. The silanol groups present on the surface of the mesopores offer a platform for the catalyst and the interconnecting micropores of the ordered mesopores makes it suitable for carbon diffusion into the pores [13, 18]. While preferring doped CNTs for supercapacitors, two types of approaches are possible, (a) direct synthesis, in which, simultaneous CNT growth and doping takes place and (b) post treatment, in which, the pre-synthesized CNT will be treated with the dopant material [19].

Electrochemical energy is a promising, clean and renewable energy source due to the increasing demand for eco-friendly and high-performance energy storage devices. Batteries, fuel cells and supercapacitors are the leading energy devices working on the principle of electrochemical energy storage and conversion [20]. Supercapacitors or ultracapacitors or electrochemical capacitors are one of the most promising energy storage devices, attracted notable attention in various fields of applications including electronics, electric vehicles and power supply devices in the last decade. They deliver high energy density and high power density than dielectric capacitors and batteries, respectively [21, 22]. So, they act as a power-energy difference between capacitors and batteries. These features made them employed in the fields of electronics, transportation and industrial applications. The attention on supercapacitors is also raised due to their long cycle life, high specific capacitance, low internal resistance, high reliability, wide temperature range and rapid charging [20, 23, 24]. Based on the energy storage mechanism, supercapacitors can be classified into electric double layer (EDLC) capacitor, in which, the electric charge is stored electrostatically or Pseudocapacitor, in which, the faradaic charge storage of electroactive species stores the energy. Combined properties of both system lead to hybrid capacitors [25, 26].

H_2SO_4 is the most usually employed aqueous electrolyte since they have high ionic concentration with a small ionic radius and thus to provide low resistance with increased capacitance and power. The preparation process in the case of this electrolyte is also simple without involving any controlled conditions [27]. Moreover, they are cost effective and easy to handle. H_2SO_4 holds very high ionic conductivity, which is one of the most essential requirements for an ideal electrolyte. Especially for the carbon materials, H_2SO_4 opt as a better electrolyte for both EDLC and pseudocapacitors. In EDLC, the ion mobility increases the electrolyte conductivity and thus increases capacitance, while in pseudocapacitors, during the redox process the protons (H^+) were involved to induce the specific capacitance [28]. The ionic radius of the cationic species in H_2SO_4 while comparing with other aqueous electrolytes like KOH and Na_2SO_4 are in the order of $H^+ < K^+ < Na^+$. Also H^+ has the highest ionic conductivity than K^+ and Na^+. Hence, the smaller ionic

radius and the higher ion conductivity of H^+ create maximum ion transportation at the electrode/ electrolyte interface enabling more energy storage performance with H_2SO_4 as an electrolyte [29].

Herein, we are reporting nitrogen and phosphorous co-doped multi-walled carbon nanotubes (N,P/CNT) produced by direct synthesis technique in the CVD method using Fe/SBA-15 as the catalytic support towards the supercapacitor electrode. Pristine CNT, nitrogen-doped CNT (N/CNT) and phosphorous-doped CNT (P/CNT) were also synthesized for the comparative study. SBA-15 was synthesized by hydrothermal method and Fe was loaded over the SBA-15 support by wet impregnation method. The catalytic support and the purified CNTs were analyzed with basic physicochemical characterization techniques. All the CNTs were investigated with a series of electrochemical measurements in three-electrode cell using 1 M H_2SO_4. N,P/CNT was further examined under a two-electrode cell by modifying it as a symmetric device.

2 Material and methods

2.1 Chemicals

The chemicals used in this work were of analytical grade and used without further purification. Triblock copolymer poly(ethylene glycol)-*block*-poly(propylene gycol)-*block*-poly(ethylene gycol) (Pluronic P123) and Tertaethyl orthosilicate (TEOS) were purchased from Sigma-Aldrich and used as the structure directing agent and silica source, respectively, for the synthesis of SBA-15. Iron(III) nitrate nonahydrate ($Fe(NO_3)_3.9H_2O$), cyclohexylamine, di-Ammonium hydrogen phosphate (($NH_4)_2HPO_4$), polyvinylidine fluoride (PVDF) and carbon black were purchased from Merck. Xylene was purchased from Fischer Scientific. Triphenylphosphine was purchased from Sigma-Aldrich. N,N-dimethyl formamide was purchased from Rankem. Hydrochloric acid, hydrofluoric acid and sulphuric acid were purchased from Merck. Aqueous solutions were prepared using double distilled (DD) water. The quartz tube with 45 mm inner diameter, 2 mm thickness and 950 mm length was used for the reaction. High-purity acetylene, H_2 and Ar gas were utilized for synthesis, reduction and to maintain the inert atmosphere during the synthesis, respectively.

2.2 Synthesis of SBA-15 and Fe/SBA-15

Santa Barbara Amorphous-15 (SBA-15) was synthesized by a hydrothermal method according to the reported procedure [30]. In a typical synthesis, 4.04 g of P123 was dissolved in 30 mL of DD water in a PP bottle and the solution was vigorously stirred for 3 h. About 120 mL of 2 N HCl was added

and allowed to continue stirring for 2 h at 40 °C. Now, 9 g of TEOS was added drop by drop to the solution and stirred for 24 h at 40 °C. The solution was then transferred to a Teflon-lined autoclave and aged at 100 °C for 48 h. The obtained product was repeatedly washed and filtered with DD water and dried at 100 °C. Then they were calcined at 550 °C for 6 h and cooled to room temperature.

10 wt% Fe was loaded on SBA-15 by wet impregnation method [18], in which, a sufficient amount of SBA-15 was dissolved in DD water by ultra-sonication. To this, Ferric nitrate nonahydrate dissolved in DD water was added and stirred continuously for 6 h at room temperature. Finally, Fe/SBA-15 was dried and calcined at 550 °C for 6 h.

2.3 Synthesis and purification of carbon nanotubes

The carbon nanotubes were synthesized by the chemical vapour deposition (CVD) method [31]. In this procedure, 100 mg of Fe/SBA-15 was evenly spread on the quartz boat and kept at the reaction zone of the quartz tube. The catalyst along with the support was purged with H_2 for reduction at 700 °C for 20 min before starting the reaction. The main synthesis was carried out at 800 °C for 2 h and the flow rate was kept as 3 mL/h. Xylene was used as the source of carbon for the synthesis of pristine CNT. Cyclohexylamine was used as the single source of carbon and nitrogen for the production of N/CNT. For P/CNT, 9:1 weight ratio of xylene and triphenylphosphine was mixed and used as the precursor for carbon and phosphorous, respectively. The precursor for the synthesis of co-doped CNTs (N,P/CNT) was acetylene gas (30 sccm) for carbon and a saturated solution of di-Ammonium hydrogen phosphate as a single source for nitrogen and phosphorous. After the reaction, the furnace was cooled to room temperature under an Ar atmosphere.

The synthesized carbon material was treated with 48% HF for the removal of the silica phase. It was further treated with 6N HCl to remove the Fe particles, washed with double distilled water and dried. Finally, the CNTs were annealed at 400 °C for 0.5 h.

2.4 Electrochemical measurements

The CNTs were made into electrodes and studied their electrochemical behaviour in three-electrode cell using 1 M aqueous H_2SO_4. Platinum wire, Ag/AgCl and the active material modified carbon felt were used as the counter, reference and working electrodes, respectively. For the preparation of the working electrode, the active material (CNTs), PVDF and carbon black were taken in 8:1:1 ratio and grinded well using DMF to make a thick paste. Then this paste was coated on the surface of carbon felt by the doctor blade method at 1×1 cm size and kept at 80 °C for 12 h. Cyclic voltammetry (CV) was carried out with varying

scan rate ranging from 5 to 100 mV/s. Electrochemical impedance spectroscopy (EIS) was attained at the frequency range of 100 kHz–0.01 Hz with 0.10 mV amplitude at the open circuit potential. Galvanostatic charge discharge (GCD) was measured at different current densities from 0.5 to 10 A/g. The potential window was kept between (− 0.2 and 0.8) V for both CV and GCD studies.

2.5 Device fabrication

Symmetric supercapacitor device was fabricated with N,P/CNT using Ballard carbon paper. For fabrication, the thick paste was prepared as discussed in three-electrode cells and spread over the carbon sheets by 1×1 cm size and dried at 80 °C for 12 h. The two dried electrodes were closely binds together keeping Whatman filter paper soaked in 1 M aqueous H_2SO_4 as the separator in between them. This device was studied with CV and GCD with the same potential window as applied in the three-electrode cells. The electrochemical measurements were carried out in Metrohm Autolab (PGSTAT 302 N) with the assistance of NOVA 1.11 software.

The specific capacitance was calculated from the GCD curves using the Eq. (1).

$$C_{sp} = \frac{I \Delta t}{m \Delta V} \qquad (1)$$

where, C_{sp}, I, Δt, ΔV and m are the specific capacitance (F/g), applied current (A), discharge time (s), potential window (V) and mass of the single working electrode (g), respectively. The energy density (E) and power density (P) were calculated for the device using the Eqs. (2) and (3), respectively.

$$E = \frac{1}{2} \frac{C_{sp}}{3.6} V^2 \qquad (2)$$

$$P = \frac{E}{t} \times 3600 \qquad (3)$$

Energy efficiency was also derived for the device from GCD curves by the calculation (4) [32]. The capacitance retention and columbic efficiency of the device were also calculated from the cyclic stability test using the relation (5) and (6), respectively.

$$\text{Energy efficiency} = \frac{\text{energy density}_{(discharge)}}{\text{energy density}_{(charge)}} \times 100 \qquad (4)$$

$$\text{Capacitane Retention} = \frac{C_{sp} \text{ of } 1^{st}/100^{th}/200^{th} \text{ cycle, etc.,}}{C_{sp} \text{ of } 1^{st} \text{ cycle}} \times 100 \qquad (5)$$

$$\text{Columbic efficiency} = \frac{t_D}{t_C} \times 100 \qquad (6)$$

2.6 Characterisation techniques

XRD patterns were performed on a PANalytical X'Pert diffractometer, in nickel-filtered CuKα as the radiation source ($\lambda = 1.54$ Å) and a solid-state detector of liquid nitrogen-cooled germanium. The diffractograms were recorded in the 2θ range of 0.5°–5° for low angle and 10°–80° for high angle. The FT-IR studies were done on a Perkin-Elmer (Spectrum RX1) instrument using a KBr pellet technique. About 200 mg of spectral grade KBr grounded with 4 mg of the sample to made into a pellet using a hydraulic press and analysed in the range of 400–4000 cm^{-1}. Raman spectra were analyzed with a Micro-Raman system using an excitation laser line at 532 nm with Nd-YAG. SEM, energy dispersive X-ray spectroscopy and elemental mapping were determined on a carl Zeiss MA 15/EBO18, where, the samples were coated with a metallic layer using Au to improve the sample contrast. HR-TEM and selected area diffraction pattern (SAED) were employed on JEOL JEM-2000 high-resolution transmission electron microscopy (HR-TEM). The sample was dispersed well in ethanol before testing. The X-ray photoelectron spectroscopy (XPS) was taken on PHI 5000 versa probe III instrument under ultra-high vacuum after cleaning the sample surface through an ion-gun etching process.

3 Results and discussion

3.1 Physicochemical characterizations

3.1.1 Characterization of catalyst

The low-angle XRD patterns of SBA-15 and Fe/SBA-15 are shown in Fig. S1(a). SBA-15 shows strong peak at 0.9° attributed to (100) and two weak peaks at 1.6° and 1.9° correspond to (110) and (200), respectively, indicating its ordered mesoporous structure. These peaks intensity get decreased in Fe/SBA-15, due to the loading of iron, which might block the pores [13].

From the wide-angle XRD pattern of SBA-15, a broad diffraction peak was observed around 23° referring to the presence of mesoporous silica material. This peak was retained even after the metal loading in Fe/SBA-15, which shows additional peaks at 33.5°, 36.1°, 50.1°, 54.9° and 65.4° credited to (104), (110), (024), (116) and (300), respectively [18]. These peaks indicate the successful loading of Fe over SBA-15 and the wide-angle XRD patterns are presented in Fig. S1(b). Thus the XRD results reveal

that Fe has loaded over SBA-15 without disturbing the mesoporous structure.

Figure S1(c) shows the FT-IR spectra of SBA-15 and Fe-loaded SBA-15. Both the material displays a band around 3400 cm^{-1} that relates to the vibration of the silanol (Si–OH) group and a band at 1640 cm^{-1} corresponds to the absorbed water molecules. The presence of Si–O–Si band at 1091 cm^{-1} was notable in both spectra. Further, the rocking and bending vibrations of Si–O–Si group were also found at 467 and 802 cm^{-1}, respectively. But the intensity of this band decreases in Fe/SBA-15, might be due to the loading of iron species [33].

Figure S2(a) and (b) are the corresponding SEM images of SBA-15 and Fe/SBA-15. Both the image shows bundles of small rod-like morphology and Fe/SBA-15 has retained the structure even after the loading of iron. All these studies articulated the formation of SBA-15 and Fe loading over it.

3.1.2 Characterization of CNTs

The XRD patterns are given in Fig. 1a. CNT displays a broad diffraction peak centered at 22.9° corresponding to (002) plane. While for the remaining samples, this peak gets shifted to 25.6°, due to the doping of heteroatoms. An additional peak around 43.7° was observed in all the samples assigned to (101) plane [34, 35]. Hence, the peaks were attributed to the graphitic plane and thus confirm the presence of carbon material.

The Raman spectra tell about the structural distortions of the CNTs and they are presented in Fig. 1b. The carbon materials show D or disorder band at 1349 cm^{-1}, telling about the presence of disorder in the nanotubes and G or graphitic band at 1590 cm^{-1}, corresponding to the E$_{2g}$ stretching vibrational modes of sp^2 hybridized carbon in the graphite layers [35, 36]. Further the I$_D$/I$_G$ ratio for each CNT was calculated and given in Table 1. The defects are due to the oxygen functionality in CNT and the dopants such as N and P in the doped CNTs. The I$_D$/I$_G$ ratio of the samples is

Fig. 1 a XRD patterns and b Raman spectra of CNTs
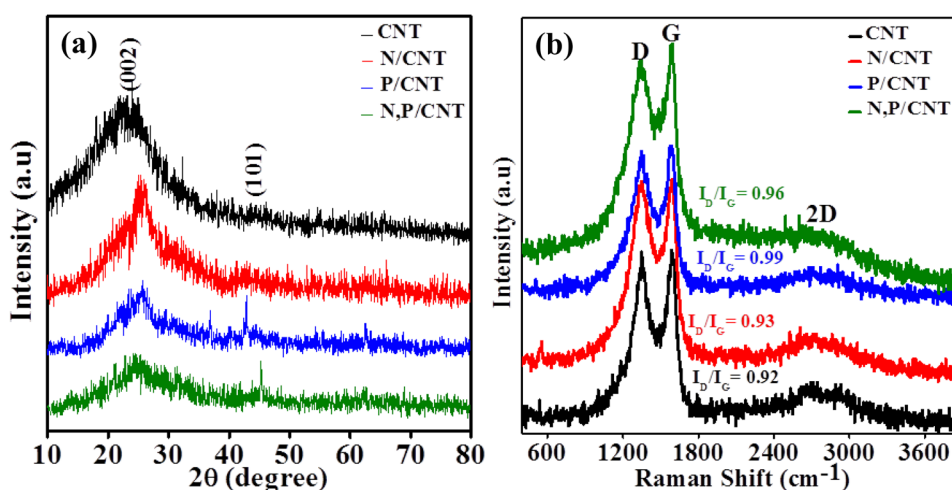
Table 1 Physicochemical and electrochemical properties of CNTs

Sample ID	I_D/I_G ratio[a]	Element content at.%[b]			R_s (Ω)[c]	R_{ct} (Ω)[d]	Bode phase angle (°)[e]	Specific capacitance (F/g)[f]
		C	O	Others				
CNT	0.92	78.74	21.26	NIL	5.4	5.2	69.9	129
N/CNT	0.93	84.50	11.82	N=3.68	4.3	4.2	77.9	297.3
P/CNT	0.99	82.92	7.35	P=9.73	4.9	4.8	76	142.6
N,P/CNT	0.96	80.91	14.51	N=3.16 P=1.42	1.1	1.0	79.2	358.2

[a]I_D/I_G ratio calculated from Raman spectra

[b]Atomic percentage of N & P governed from SEM/EDAX results

[c]Equivalent series resistance or solution resistance

[d]Charge transfer resistance calculated from EIS—Nyquist Plot

[e]Phase angle from EIS- Bode plot

[f]Specific capacitance determined from GCD using the equation $C_{sp} = I\Delta t/m\Delta V$

in the order as P/CNT > N,P/CNT > N/CNT > CNT. Greater the defect, the greater the I_D/I_G ratio, which is coinciding with the EDAX results also. Also an additional band was observed around 2700 cm^{-1} attributed to 2D band, which also tells about the presence of defects in the CNTs [37]. Thus the presence of defective graphitic carbon was expressed by Raman spectra.

The morphology of the materials was examined by SEM and HR-TEM images. Figure 2 shows the SEM images of CNTs, where, they display long tubular structures. But in the case of phosphorous-doped CNT, the formation of the tubular structure was low compared with the other CNTs, which is shown in Fig. 2e, f. That is phosphorous doping suppresses the formation of nanotubes and makes them shorter in length [7]. Hence, SEM images reveal the nanotube morphology of the carbon materials. Further, the EDAX spectra of the CNTs presented in Fig. S3 tells the presence of N (3.68 at.%) in N/CNT, P (9.73 at.%) in P/CNT and N (3.16 at.%) & P (1.42 at.%) in N,P/CNT and their corresponding elemental compositions are given in the inset of Fig. S3. Also, the elemental mapping of N,P/CNT is attached in Fig. 2, which, further supports the presence of N and P in N,P/CNT.

The HR-TEM images at different magnifications of N,P/CNT are displayed in Fig. 3. The images confirm the presence of nanotubes and they were found to be multi-walled (Fig. 3f) and the inner compartment of the tubes was cone stack-bamboo-like shaped, which are clearly seen in Fig. 3e. The blue line shows the open end of the nanotubes, created might be due to the removal of metal particles during purification step. These open ends further pay way for the diffusion of more ions to further increase the capacitance. Additionally, the SAED pattern of N,P/CNT is given in the inset of Fig. 3f, where, ring-like pattern along with randomly distributed spots were noticed. The ring-like pattern arises owing to the polycrystalline nature of the nanotubes and the bright spots might due to the presence of heteroatoms [32].

The composition and the bonding of the elements present in N,P/CNT were attained by XPS. The survey spectrum given in Fig. 4a tells the presence of N and P and their composition were 2.0 and 0.9 at.%, respectively. The peaks attained at 284, 531, 399 and 132 eV were corresponded to C 1s, O 1s, N 1s and P 2p, respectively [38]. In the deconvoluted peak of C 1s, given in Fig. 4b, the most intense peak at 284 eV is attributed to C=C bond of sp^2 hybridized carbon of the nanotubes. The additional peak at 285.4 eV
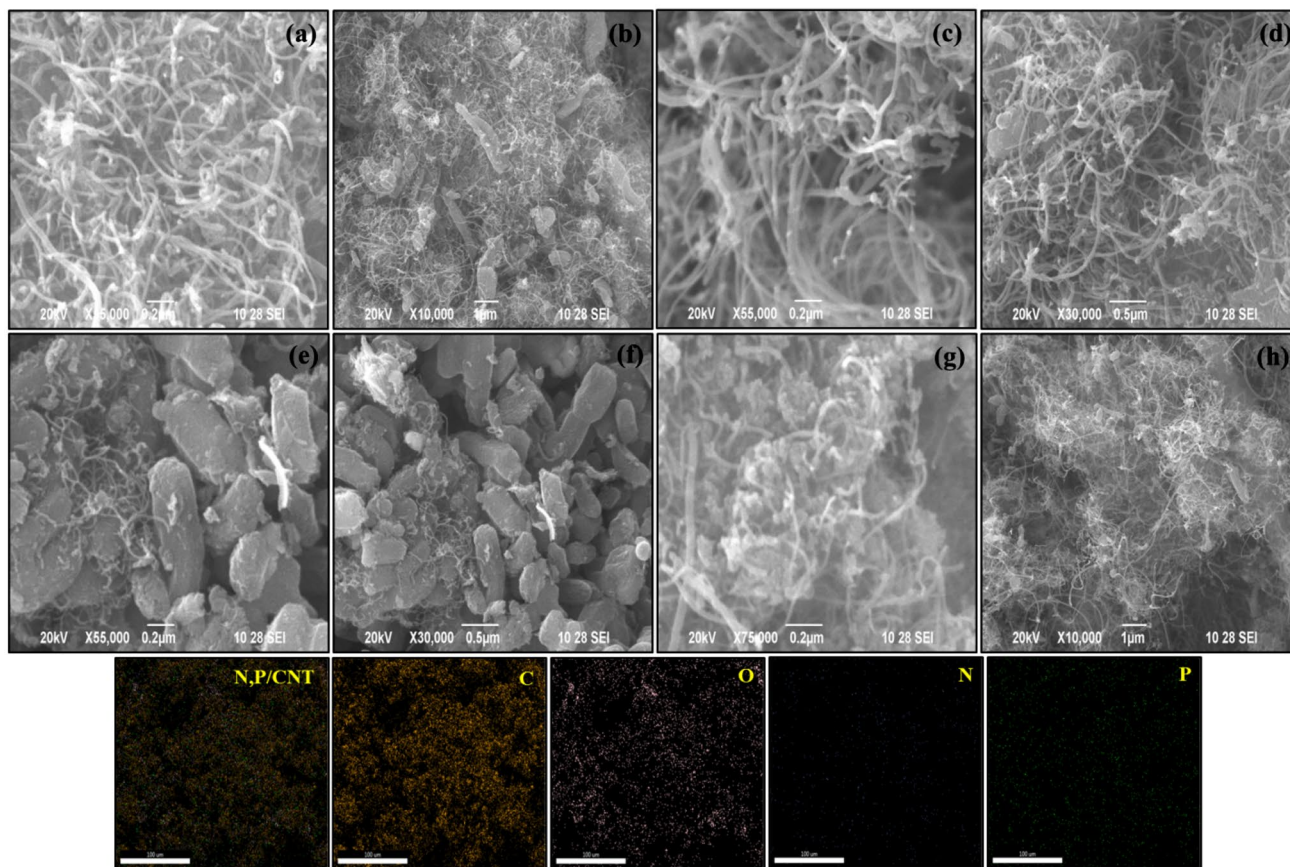
Fig. 2 SEM images of **a**, **b** CNT, **c**, **d** N/CNT, **e**, **f** P/CNT and **g**, **h** N,P/CNT and elemental mapping of N,P/CNT
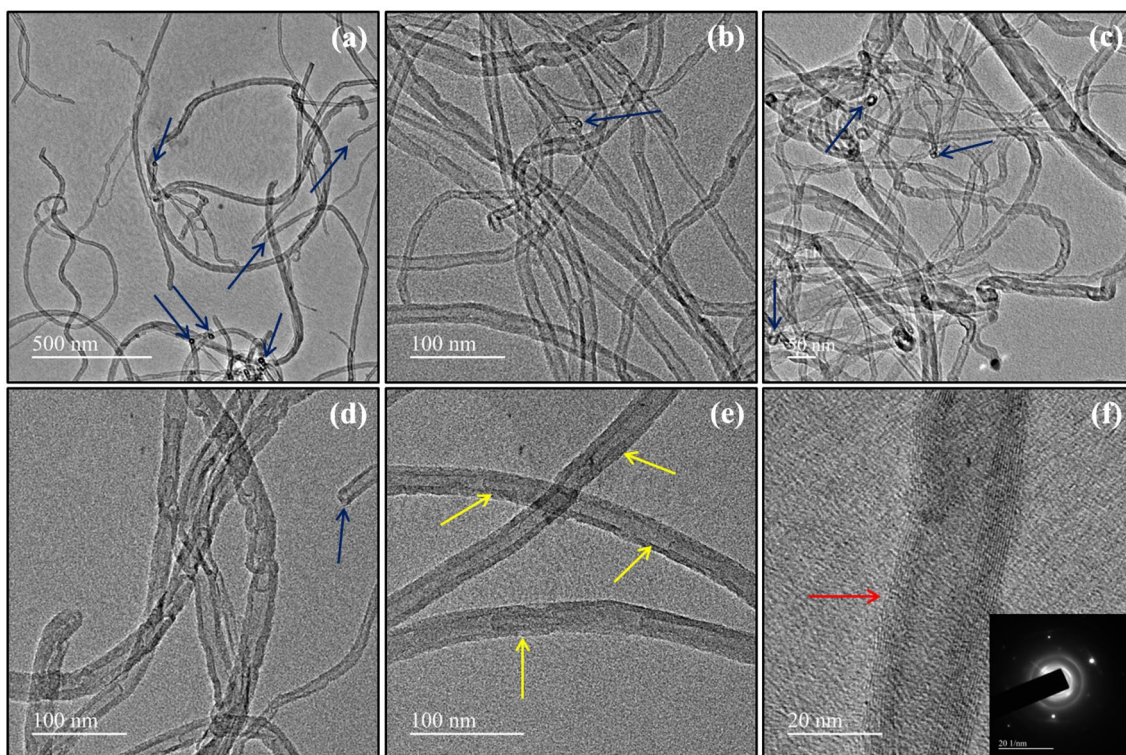
Fig. 3 HR-TEM images at different magnification and (f-inset) SAED pattern of N,P/CNT

is assigned to C-O bonding and the other peak at 287.6 eV can be credited to either C=O or C=N bond, where this peak reveals the incorporation of N in the carbon framework [39]. Similarly, the resolved peak of O 1s is shown Fig. 4c and their corresponding elemental bonding is connived in the figure. The resolved N 1s peak is displayed in Fig. 4d and it consists of three types of bonding configuration of nitrogen, they are pyridinic N (398.0 eV), pyrrolic N (399.2 eV) and quartney N (400.7 eV) [39, 40]. The de-convoluted peak of P 2p presented in Fig. 4e shows a peak at 132.4 eV ascribed to the bonding of P–C [41, 42]. Thus the XPS study confirms the doping of N and P in the nanotube's carbon framework.

3.2 Electrochemical studies

Figure 5a shows the CV loops of CNTs in the scan rate of 5 mV/s at the potential window of 1 V. It is noticeable from the figure that, the CV loops of CNT were rectangular, indicating the charge storage mechanism is favored by EDLC behaviour. While in the case of doped CNTs, the loops were deviating from the rectangular regularity, showing the charge storage contribution is due to both EDLC and pseudo behaviour. The favored EDLC behaviour is due to the carbon structure and pseudo behaviour arises due to the dopants along with the oxygen functionalities. The observed redox peaks are around 0.34, 0.27 & −0.03 V for N/CNT;

0.33 & 0.27 V for P/CNT and 0.37, 0.31 & 0.04 V for N,P/CNT. The elements N and P are rich in electrons, during the energy storage process, the excess electron from these elements enrolls in the charge accumulation at the electrode/electrolyte interface leading to electrolytic charge storage. In the case of pseudo behavior, these electrons combine with the oxygen functionalities and the protons from electrolyte to form simultaneous oxidation and reduction of the faradic redox reaction leading to electrochemical charge storage, thus forming the redox peaks in the CV curves of the doped CNTs. Further, considering the area under the curve, it was higher for N and P co-doped CNTs, telling its charge storage capacity is greater when comparedth the other CNTs. The CV loops of N/CNT and P/CNT were higher than the undoped CNT, demonstrating that the doping of heteroatom has increased the storage capacity. When comparing with N/CNT and P/CNT, nitrogen doping is more effective in increasing the capacitance than phosphorus, while in N,P/CNT, the synergic effect of N and P has further increased the capacitance. Moreover, the CV loops of all the samples at varying scan rates ranging from 5 to 100 mV/s are given in Fig. S4. They exhibit consistent CV loops at all the scan rates.

The specific capacitance was calculated from the GCD studies. The GCD curves carried out at 0.5 A/g current density with the same potential window as that of CV are
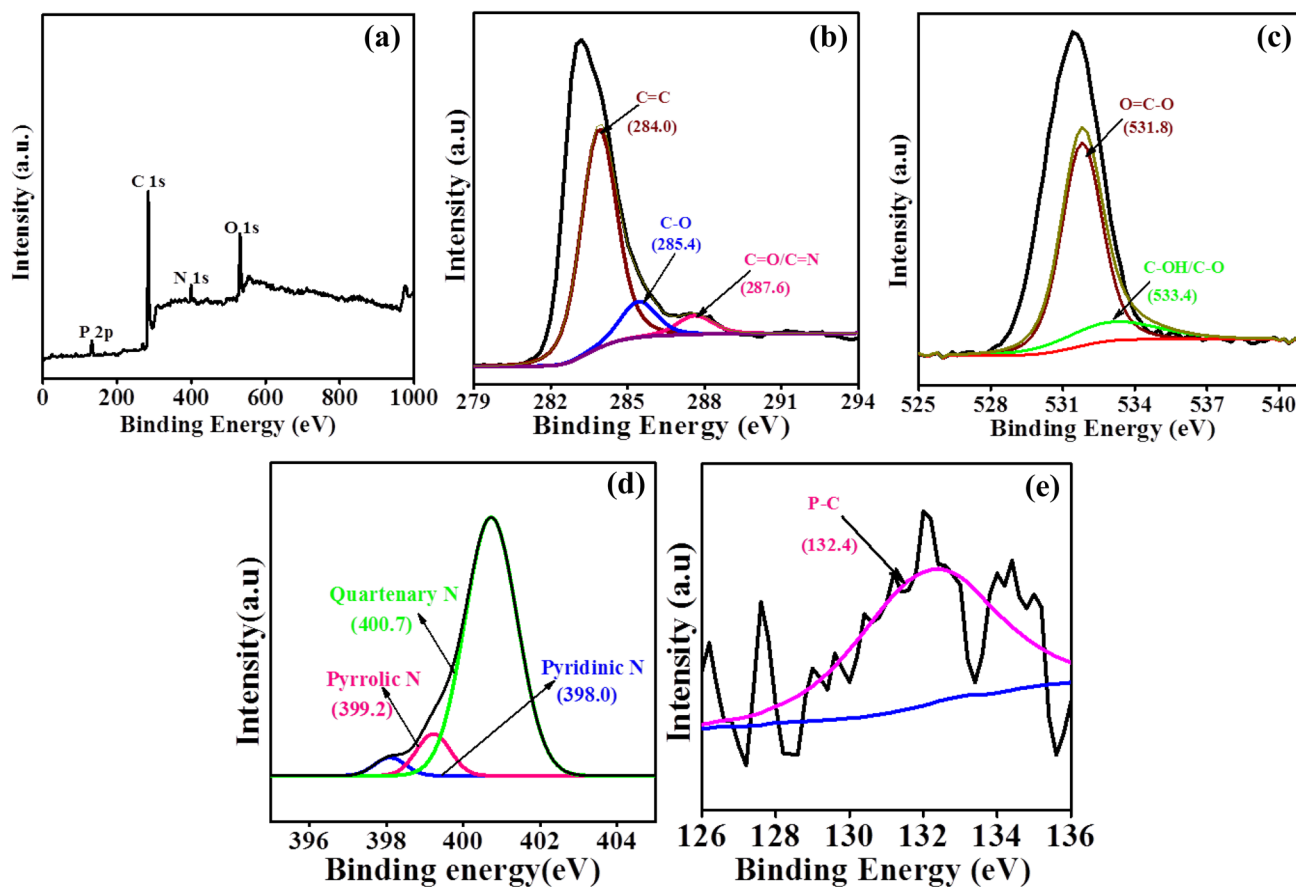
Fig. 4 XPS of N,P/CNT **a** survey spectrum, de-convoluted **b** C 1s, **c** O 1s, **d** N 1s and **e** P 2p peaks

displayed in Fig. 5b. Regular triangular wave was observed for CNT, while the irregular triangular wave was detected for all other doped CNTs, representing that the dopants have created the irregularity. That is, the charge storage mechanism of CNT is by EDLC and the doped CNTs are due to both EDLC and pseudo behaviour as discussed in CV. Figure 5c shows the discharge profiles at the current density of 0.5 A/g. The co-doping effect leads to a higher discharge second of N,P/CNT which further leads to the higher specific capacitance. The specific capacitance was calculated using Eq. (1) and a plot between current density and specific capacitance is given in Fig. 5d. The calculated specific capacitance of CNT, N/CNT, P/CNT and N,P/CNT were 129, 297.3, 142.6 and 358.2 F/g, respectively, at 0.5 A/g current density. Also, the values are listed in Table1. Further, the GCD and discharge profiles at the different current densities are given in Fig. S5 and S6, respectively.

The resistance of the materials was studied by the EIS technique at the frequency range of 100 kHz–0.01 Hz with 0.10 mV amplitude at the open circuit potential. From the Nyquist plot, presented in Fig. 6a, the solution resistance

(R_s) or equivalent series resistance of N,P/CNT was found to be 1.1 Ω. Also, the charge transfer resistance (R_{ct}) of N,P/CNT was 1.0 Ω. The resistance of N,P/CNT was found to be low, indicating its high capacitive nature while comparing with the other materials. The resistance values of all the samples are given in Table 1. Bode plot or the phase angle plot is the secondary one for the discussion of the resistivity of the materials along with the Nyquist plot. It is the plot between the logarithms of frequency versus the measured phase angle values. The resistivity of the material will be debated from the phase angle at the low frequency region. It is said that, for an ideal capacitor, the phase angle would reach 90° [43–45]. The Bode plot of all the CNTs is shown in Fig. 6b. The phase angle of N,P/CNT reaches a maximum (79.2°) at 10 mHz AC frequency comparatively with other CNTs, suggesting that N,P/CNT performs more like an ideal capacitor than the others. Thus, N,P/CNT shows low resistance and the EIS findings were consistent with CV and GCD results. The phase angle values of all the samples are also mentioned in Table 1.

Fig. 5 **a** CV curves of CNTs at
5 mV/s scan rate, **b** GCD pro-
files and **c** discharge profiles of
CNTs at 0.5 A/g current density
and **d** specific capacitance as a
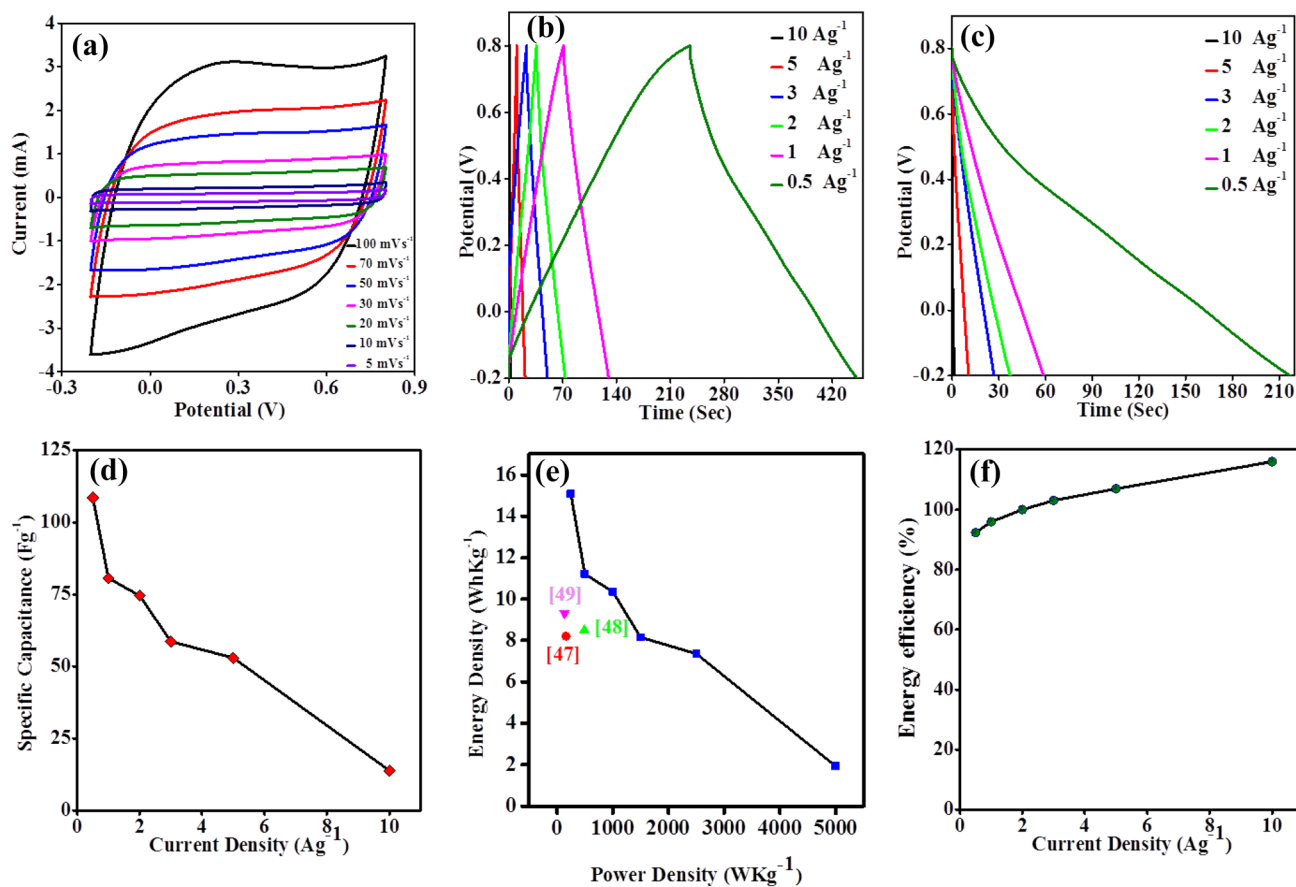function of current density in
three-electrode cells
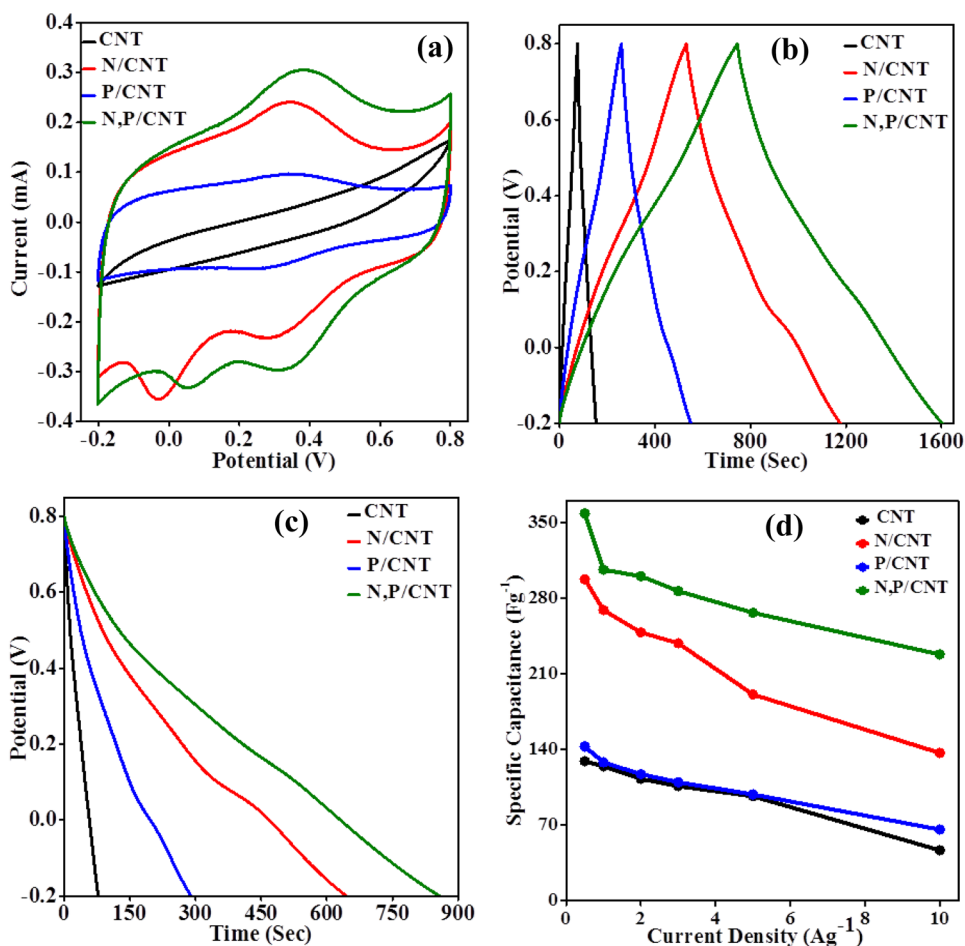
Fig. 6 **a** EIS Nyquist plot and
b Bode phase plot of CNTs in
three-electrode cells
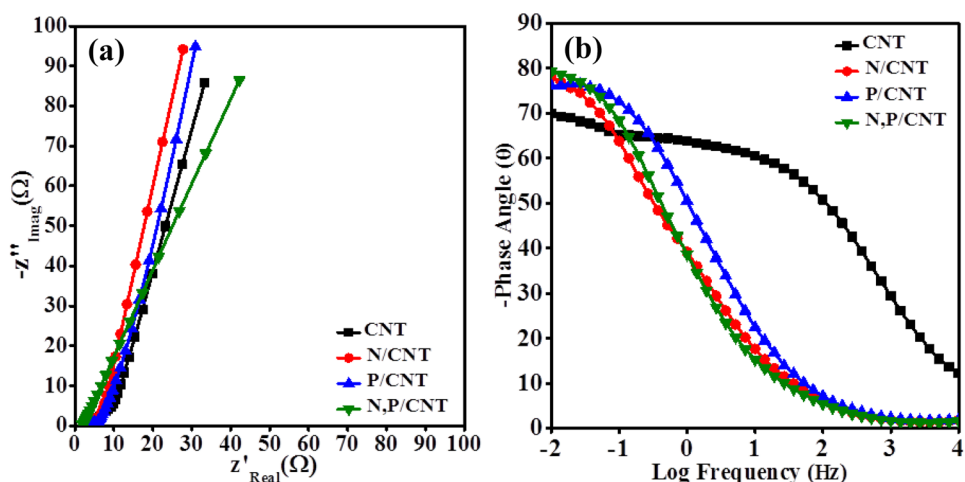
3.3 Symmetric device

N,P/CNT was further fabricated into a symmetric device and
studied its electrochemical properties. The CV and GCD
studies were carried out with the same potential window
as that of the three-electrode. The CV loops of the device
at different scan rates are shown in Fig. 7a. The rectangular
shape of the CV loops was maintained even at higher scan
rates also, showing the rapid ion transportation. The GCD
and discharge profiles of the device at different current den-
sity are shown in Fig. 7b, c. The specific capacitance was
calculated from a GCD study using Eq. (1). N,P/CNT device
delivers a specific capacitance of about 108.6 F/g at 0.5 A/g.
The plot between current density and its corresponding

Fig. 7 **a** CV curves at different scan rates, **b** GCD at different current densities, **c** discharge profiles at different current densities, **d** specific capacitance as a function of current density, **e** Ragone plot compared with reported literatures [47–49] and **f** energy efficiency of the symmetric N,P/CNT supercapacitor device

specific capacitance was given in Fig. 7d. Also, the energy density and power density of the device was calculated using Eqs. (2) and (3), respectively. The device delivers 15 Wh/kg energy density and 250 W/kg power density at 0.5 A/g. The Ragone plot between power density and energy density at varying current density is shown in Fig. 7e. Energy efficiency is a significant parameter to consider an electrode material for practical application. The energy efficiency of the device was calculated using relation (4) and it was 92.3% at 0.5 A/g. The plot of current density Vs energy efficiency is also displayed in Fig. 7f. From the figure, it is noticeable that the energy efficiency increases with the increase of current density, due to the fact that the average potentials upon charging and discharging are equal at the higher current density, also when lowering the current density, these potentials goes on decreasing [46].

The stability of the device was carried out with a cyclic stability test at 3 A/g for 5000 charge–discharge cycles. 96.2% of capacitance was retained by the device after the stability test and it is given in Fig. 8a. The capacitance retention was calculated using Eq. (5). In addition, the inset of Fig. 8a shows the first and last ten cycles of the stability test. The specific capacitance and columbic efficiency (calculated using Eq. 6), of the device were calculated for every hundredth cycle and plotted Vs cycle number in Fig. 8b. The columbic efficiency of the device was 90.6% at 5000th cycle. A CV loop of the device before and after 5000 cycles was carried out at the scan rate of 100 mV/s and it is displayed in the inset of Fig. 8b. Thus, the cycling test indicates the electrochemical stability of the material.

The calculated values of the N,P/CNT symmetric supercapacitor device are listed in Table S1. Also, a comparative list of electrochemical data of some similar materials with the present work is given in Table 2. Co-doping with N and P create negative sites since N and P are electron-rich elements than carbon. So, when they are introduced into the carbon lattice of CNTs, they release their excess electrons to carbon creating n-type doping. Thus, the synergetic contribution of N and P co-doping provides fast ion transportation reactions which further improve the supercapacitive performance of the nanotubes.
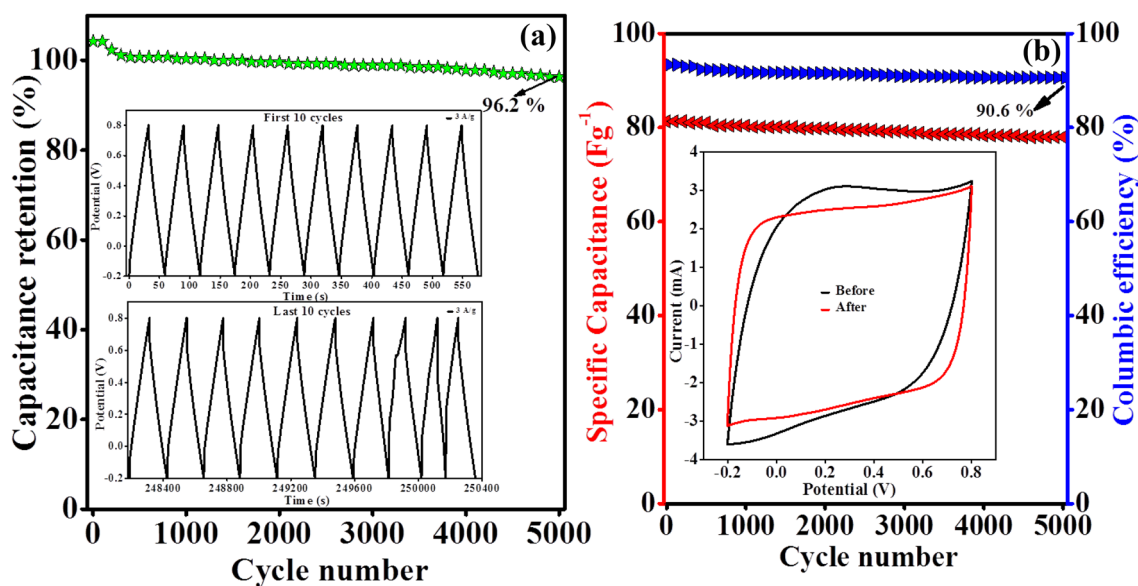
Fig. 8 **a** Capacitance retention as a function of cycle number, (a-inset) first and last ten cycles of cycling test and **b** specific capacitance and Columbic efficiency as a function of cycle number, (b-inset) CV curve at 100 mV/s scan rate before and after 5000 cycles of the symmetric N,P/CNT supercapacitor device

Table 2 Comparison of electrochemical data of some recent similar materials with the present work

S. no.	Electrode	Electrolyte	Specific capacitance (three-electrode)	Specific capacitance (two-electrode)	Energy density an power density	Capacitance retention	References
1	N doped coiled double-walled carbon nanotubes	0.5 M H_2SO_4	51.29 F/g (0.125 A/g)	–	7.757 Wh/kg and 0.549 kW/kg	–	[50]
2	P, N and O co-doped polymer-based core–shell carbon sphere	1.0 M H_2SO_4	–	157 F/g (0.05 A/g)	10 Wh/kg and 750 W/kg	15% decrease after 5000 cycles	[12]
3	N doped CNTs	1.0 M H_2SO_4	295 F/g (0.5 A/g)	–	–	–	[28]
4	Vertical aligned CNTs and polyaniline nanocomposite	1.0 M $HClO_4$	–	403.3 F/g (1 A/g)	98.1 Wh/kg	90.2% after 3000 cycles	[21]
5	P and N dual-doped microporous carbon	6 M KOH	183.8 F/g (1 A/g)	–	–	90%	[34]
6	N and P co-doped porous carbon	6 M KOH	340.2 F/g (1 A/g)	227.2 F/g (1 A/g)	26.289 Wh/kg and 3694.084 W/kg	94.2% after 10,000 cycles	[35]
7	P and N co-doped porous exfoliated carbon nanosheets	6 M KOH	–	265 F/g (0.5 A/g)	–	94% after 5000 cycles	[38]
8	N,P co-doped porous carbon	6 M KOH	265.8 F/g (0.2 A/g)	167.7 F/g (1 A/g)	14.912 Wh/kg and 800 W/kg	98% after 10,000 cycles	[41]
9	P and N dual-doped mesoporous carbon	1.0 M H_2SO_4 & 6 M KOH	272 F/g 236 F/g (0.2 A/g)	–	38.2 Wh/kg and 204.6 W/kg	–	[51]
10	N and P co-doped CNTs	1.0 M H_2SO_4	358.2 F/g (0.5 A/g)	108.6 F/g (0.5 A/g)	15 Wh/kg and 250 W/kg	96.2% after 5000 cycles	This work

4 Conclusions

In this work, we report nitrogen and phosphorous co-doped carbon nanotubes by direct synthesis in the CVD method using Fe/SBA-15. Basic characterization studies reveal the formation of nanotubes with a reasonable amount of heteroatom doping. The elemental composition of N and P from the XPS study were found to be 2.0 and 0.9 at.%. As per the SEM study, phosphorous doping has limited the formation of nanotubes. In additon, P doping created only a minimal increase in the capacitance as noted from the three-electrode study. Further, N,P/CNT gave a maximum specific capacitance of 358.2 F/g at 0.5 A/g current density. The N,P/CNT symmetric supercapacitor device delivered a specific capacitance of 108.6 F/g with an energy density of 15 Wh/kg and power density of 250 W/kg at the current density of 0.5 A/g. In addition, the observed energy efficiency of the device was 92.3% with 96.2% of capacitance retention and 90.6% of coulombic efficiency for over 5000 charge–discharge cycles. Thus the N and P co-doped carbon nanotubes would be an effective electrode material for consideration under supercapacitor energy storage devices.

Declarations

Conflict of interest This work has no conflict of interest to declare.

References

1. Anzar N, Hasan R, Tyagi M, Yadav N, Narang J (2020) Carbon nanotube—a review on synthesis, properties and plethora of applications in the field of biomedical science. Sensors Int 1:100003. https://doi.org/10.1016/j.sintl.2020.100003

2. Candelaria SL, Shao Y, Zhou W, Li X, Xiao J, Zhang J, Wang Y, Liu J, Li J, Cao G (2012) Nanostructured carbon for energy storage and conversion. Nano Energy 1:195–220. https://doi.org/10.1016/j.nanoen.2011.11.006

3. Allen BL, Kichambare PD, Star A (2008) Synthesis, charcterization and manipulation of nitrogen-doped carbon nanotube cups. ACS Nano 2:1914–1920

4. Chizari K, Vena A, Laurentius L, Sundararaj U (2013) The effect of temperature on the morphology and chemical surface properties of nitrogen-doped carbon nanotubes. Carbon 68:369–379. https://doi.org/10.1016/j.carbon.2013.11.013

5. Kokarneswaran M, Selvaraj P, Ashokan T, Perumal S (2020) Discovery of carbon nanotubes in sixth century BC potteries from Keeladi, India. Sci Rep 10:1–6. https://doi.org/10.1038/s41598-020-76720-z

6. Iqbal S, Khatoon H, Pandit AH, Ahmad S (2019) Recent development of carbon based materials for energy storage devices. Mater Sci Energy Technol 2:417–428. https://doi.org/10.1016/j.mset.2019.04.006

7. Larrude DG, Costa MEHM, Monteiro FH, Pinto AL, Freire FL (2012) Characterization of phosphorus-doped multiwalled carbon nanotubes. J Appl Phys 111:064315. https://doi.org/10.1063/1.3695452

8. Zhang ZJ, Zheng QC, Sun L, Xu D, Chen XY (2017) Two-dimensional carbon nanosheets for high-performance supercapacitors: large-scale synthesis and codoping with nitrogen and phosphorus. Ind Eng Chem Res 56:12344–12353. https://doi.org/10.1021/acs.iecr.7b03022

9. Cruz-silva E, Cullen DA, Gu L, Romo-herrera JM, Munoz-sandoval E, Lopezurias F, Sumpter BG, Meunier V, Charlier J, Smith DJ, Terrones H, Terrones M (2008) Heterodoped nanotubes: theory, synthesis, characteisation of phosphorous–nitrogen doped multiwalled carbon nanotubes. ACS Nano 2:441–448

10. Vinodh R, Babu RS, Gopi CVVM, Deviprasath C, Atchudan R, Samyn LM, Barros ALF, Kim HJYM (2020) Influence of annealing temperatutre in nitrogen doped porous carbon balls derived from hypercross-linked polymer of anthracene for supercapacitor applications. J Energy Storage 28:101196

11. Cruz-silva E, Lopez-urias F, Munoz-sandoval E, Sumpter BG, Terrones H, Charlier J, Terrones M (2011) Phosphorus and phosphorus–nitrogen doped carbon nanotubes for ultrasensitive and selective molecular detection. Nanoscale 3:1008–1013. https://doi.org/10.1039/c0nr00519c

12. Huang C, Puziy AM, Poddubnaya OI, Hulicova-jurcakova D, Sobiesiak M, Gawdzik B (2018) Phosphorus, nitrogen and oxygen co-doped polymer-based core-shell carbon sphere for high-performance hybrid supercapacitors. Electrochim Acta 270:339–351. https://doi.org/10.1016/j.electacta.2018.02.115

13. Balamurugan J, Pandurangan A, Thangamuthu R, Senthilkumar SM (2013) Effective synthesis of well-graphitized carbon nanotubes on bimetallic SBA-15 template for use as counter electrode in dye-sensitized solar cells. Ind Eng Chem Res 52:384–393

14. Ortega-Cervantez C, Rueda-Morales G, Ortiz-Lopez J (2005) Catalytic CVD production of carbon nanotubes using ethanol. Microelectronics J 36:495–498. https://doi.org/10.1016/j.mejo.2005.02.062

15. Somanathan T, Pandurangan A (2010) Helical multiwalled carbon nanotubes (h-MWCNTs) synthesized by catalytic chemical vapor deposition. New Carbon Mater 25:175–180. https://doi.org/10.1016/S1872-5805(09)60024-X

16. Dundar-tekkaya E, Karatepe N (2011) Production of carbon nanotubes by iron catalyst. Int J Mater Metall Eng 5:541–547

17. Hoyos-Palacio L, Garcia A, Perez-Robles J, Gonzalez J, Martinez-Tejada HV (2014) Catalytic effect of Fe, Ni, Co and Mo on the CNTs production. IOP Conf Ser Mater Sci Eng 59:012005

18. Ragavan R, Pandurangan A (2017) Facile synthesis and supercapacitor performances of nitrogen doped CNTs grown over mesoporous Fe/SBA-15 catalyst. New J Chem 41:11591–11599. https://doi.org/10.1039/c7nj00804j

19. Wang Z, Jia R, Zheng J, Zhao J, Li L, Song J, Zhu Z (2011) Nitrogen-promoted self-assembly of n-doped carbon nanotubes and their intrinsic catalysis for oxygen reduction in fuel cells. ACS Nano 5:1677–1684

20. Poonam SK, Arora A, Tripathi SK (2019) Review of supercapacitors: materials and devices. J Energy Storage 21:801–825. https://doi.org/10.1016/j.est.2019.01.010

21. Wu G, Tan P, Wang D, Li Z, Peng L, Hu Y, Wang C, Zhu W, Chen S, Chen W (2017) High-performance supercapacitors based on electrochemical-induced vertical-aligned carbon nanotubes and polyaniline nanocomposite electrodes. Sci Rep 7:1–8. https://doi.org/10.1038/srep43676

22. Frackowiak E, Abbas Q (2013) Carbon/carbon supercapacitors. J Energy Chem 22:226–240. https://doi.org/10.1016/S2095-4956(13)60028-5

23. Liu C, Liu Y, Yi T, Hu C (2019) Carbon materials for high-voltage supercapacitors. Carbon 145:529–548. https://doi.org/10.1016/j.carbon.2018.12.009

24. Rangom Y, Tang XS, Nazar LF (2015) Carbon nanotube-based supercapacitors with excellent ac line filtering and rate capability via improved interfacial impedance. ACS Nano 9:7248–7255

25. Pan H, Li J, Ping Y (2010) Carbon nanotubes for supercapacitor. Nanoscale Res Lett 5:654–668. https://doi.org/10.1007/s11671-009-9508-2

26. Gonzalez A, Goikolea E, Andoni J, Mysyk R (2016) Review on supercapacitors: technologies and materials. Renew Sustain Energy Rev 58:1189–1206. https://doi.org/10.1016/j.rser.2015.12.249

27. Wang G, Zhang L, Zhang J (2012) A review of electrode materials for electrochemical supercapacitors. Chem Soc Rev 41:797–828. https://doi.org/10.1039/c1cs15060j

28. Zhong C, Deng Y, Hu W, Qiao J, Zhang L, Zhang J (2015) A review of electrolyte materials and compositions for electrochemical supercapacitors. Chem Soc Rev 44:7484–7539. https://doi.org/10.1039/c5cs00303b

29. Pal B, Yang S, Ramesh S, Thangadurai V, Jose R (2019) Electrolyte selection for supercapacitive devices: a critical review. Nanoscale Adv 1:3807–3835. https://doi.org/10.1039/c9na00374f

30. Zhao D, Feng J, Huo Q, Melosh N, Fredrickson G, Chmelka B, Stucky G (1998) Triblock copolymer syntheses of mesoporous silica with periodic 50 to 300 angstrom pores. Science 279:548–552

31. Atchudan R, Pandurangan A, Somanathan T (2009) Bimetallic mesoporous materials for high yield synthesis of carbon nanotubes by chemical vapour deposition techniques. J Mol Catal A Chem 309:146–152. https://doi.org/10.1016/j.molcata.2009.05.010

32. Johnsirani D, Pandurangan A (2020) Chromium, fluorine and nitrogen tri-doped graphene sheets as an active electrode material for symmetric supercapacitors. Diam Relat Mater 105:107800. https://doi.org/10.1016/j.diamond.2020.107800

33. Huang H, Ji Y, Qiao Z, Zhao C, He JZH (2010) Preparation, characterization, and application of magnetic Fe-SBA-15 mesoporous silica molecular sieves. J Autom Methods Manag Chem 2010:1–7

34. Wang C, Zhou Y, Sun L, Wan P, Zhang X, Qiu J (2013) Sustainable synthesis of phosphorus- and nitrogen-co-doped porous carbons with tunable surface properties for supercapacitors. J Power Sources 239:81–88. https://doi.org/10.1016/j.jpowsour.2013.03.126

35. Zhou J, Ye S, Zeng Q, Yang H, Chen J, Guo Z, Jiang H, Rajan K (2020) Nitrogen and phosphorus co-doped porous carbon for for high-performance supercapacitors. Front Chem 8:1–8. https://doi.org/10.3389/fchem.2020.00105

36. Kishore C, Pandurangan A (2014) Facile synthesis of carbon nanotubes and their use in the fabrication of resistive switching memory device. RSC Adv 4:9905–9911. https://doi.org/10.1039/c3ra45359f

37. Zafar Z, Ni ZH, Wu X, Shi ZX, Nan HY, Bai J, Sun LT (2013) Evolution of Raman spectra in nitrogen doped graphene. Carbon 61:57–62. https://doi.org/10.1016/j.carbon.2013.04.065

38. Jin J, Qiao X, Zhou F, Wu Z, Cui L, Fan H (2017) Interconnected phosphorus and nitrogen codoped porous exfoliated carbon nanosheets for high-rate supercapacitors. ACS Appl Mater Interfaces 9:17317–17325. https://doi.org/10.1021/acsami.7b00617

39. Daems N, Sheng X, Vankelecom IFJ, Pescarmona PP (2015) Metal-free doped carbon materials as electrocatalysts for the oxygen reduction reaction. J Mater Chem A 2:4085. https://doi.org/10.1039/C3TA14043A

40. Yao Y, Zhang B, Shi J, Yang Q (2015) Preparation of nitrogen-doped carbon nanotubes with different morphologies from melamine-formaldehyde resin. ACS Appl Mater Interfaces 7:7413–7420. https://doi.org/10.1021/acsami.5b01233

41. Li X, Lv Z, Wu M, Li X, Li Z (2021) N, P co-doped porous carbon from cross-linking cyclophosphazene for high-performance supercapacitors. J Electroanal Chem 881:114952. https://doi.org/10.1016/j.jelechem.2020.114952

42. Qiao X, Liao S, You C, Chen R (2015) Phosphorus and nitrogen dual doped and simultaneously reduced graphene oxide with high surface area as efficient metal-free electrocatalyst for oxygen reduction. Catalysts 5:981–991. https://doi.org/10.3390/catal5020981

43. Laschuk NO, Easton EB, Zenkina OV (2021) Reducing the resistance for the use of electrochemical impedance spectroscopy analysis in materials chemistry. RSC Adv 11:27925–27936. https://doi.org/10.1039/d1ra03785d

44. Basnayaka PA, Ram MK, Stefanakos L, Kumar A (2013) Graphene/polypyrrole nanocomposite as electrochemical supercapacitor electrode: electrochemical impedance studies. Graphene 2:81–87. https://doi.org/10.4236/graphene.2013.22012

45. Lazanas AC, Prodromidis MI (2023) Electrochemical impedance spectroscopy—a tutorial. ACS Meas Sci Au. https://doi.org/10.1021/acsmeasuresciau.2c00070

46. Eftekhari A (2017) Energy efficiency: a critically important but neglected factor in battery research. Sustain Energy Fuels 1:2053–2060. https://doi.org/10.1039/c7se00350a

47. Xia K, Huang Z, Zheng L, Han B, Gao Q, Zhou C, Wang H, Wu J (2017) Facile and controllable synthesis of N/P co-doped graphene for high-performance supercapacitors. J Power Sources 365:380–388. https://doi.org/10.1016/j.jpowsour.2017.09.008

48. Li Z, Wang Y, Xia W, Gong J, Jia S, Zhang J (2020) Nitrogen, phosphorus and sulfur co-doped pyrolyzed bacterial cellulose nanofibers for supercapacitors. Nanomaterials 10:1–13. https://doi.org/10.3390/nano10101912

49. Chen B, Wu W, Li C, Wang Y, Zhang Y, Fu L, Zhu Y, Zhang L, Wu Y (2019) Oxygen/phosphorus co-doped porous carbon from cicada slough as high-performance electrode material for supercapacitors. Sci Rep 9:1–8. https://doi.org/10.1038/s41598-019-41769-y

50. Thirumal V, Pandurangan A, Jayavel R, Krishnamoorthi SR, Ilangovan R (2016) Synthesis of nitrogen doped coiled double walled carbon nanotubes by chemical vapor deposition method for supercapacitor applications. Curr Appl Phys 16:816–825. https://doi.org/10.1016/j.cap.2016.04.018

51. Nasini UB, Gopal V, Ramashagayam SK, Bourdo SE, Viswanathan T, Shaikh AU (2014) Phosphorous and nitrogen dual heteroatom doped mesoporous carbon synthesized via microwave method for supercapacitor application. J Power Sources 250:257–265. https://doi.org/10.1016/j.jpowsour.2013.11.014